

See discussions, stats, and author profiles for this publication at: <https://www.researchgate.net/publication/273470973>

Weaving a two-dimensional fishing net from titanoniobate nanosheets embedded with Fe_3O_4 nanocrystals for highly efficient capture and isotope labeling of phosphopeptides

ARTICLE in NANOSCALE · MARCH 2015

Impact Factor: 7.39 · DOI: 10.1039/c4nr07041k · Source: PubMed

CITATION

1

READS

24

5 AUTHORS, INCLUDING:



Xueqin Chen

Nanjing University

5 PUBLICATIONS 16 CITATIONS

SEE PROFILE



Qianhao Min

Nanjing University

15 PUBLICATIONS 330 CITATIONS

SEE PROFILE

Cite this: *Nanoscale*, 2015, 7, 5815

Weaving a two-dimensional fishing net from titanoniobate nanosheets embedded with Fe₃O₄ nanocrystals for highly efficient capture and isotope labeling of phosphopeptides†

Xueqin Chen, Siyuan Li, Xiaoxia Zhang, Qianhao Min* and Jun-Jie Zhu

Qualitative and quantitative characterization of phosphopeptides by means of mass spectrometry (MS) is the main goal of MS-based phosphoproteomics, but suffers from their low abundance in the large haystack of various biological molecules. Herein, we introduce two-dimensional (2D) metal oxides to tackle this biological separation issue. A nanocomposite composed of titanoniobate nanosheets embedded with Fe₃O₄ nanocrystals (Fe₃O₄-TiNbNS) is constructed via a facile cation-exchange approach, and adopted for the capture and isotope labeling of phosphopeptides. In this nanoarchitecture, the 2D titanoniobate nanosheets offer enlarged surface area and a spacious microenvironment for capturing phosphopeptides, while the Fe₃O₄ nanocrystals not only incorporate a magnetic response into the composite but, more importantly, also disrupt the restacking process between the titanoniobate nanosheets and thus preserve a greater specific surface for binding phosphopeptides. Owing to the extended active surface, abundant Lewis acid sites and excellent magnetic controllability, Fe₃O₄-TiNbNS demonstrates superior sensitivity, selectivity and capacity over homogeneous bulk metal oxides, layered oxides, and even restacked nanosheets in phosphopeptide enrichment, and further allows *in situ* isotope labeling to quantify aberrantly-regulated phosphopeptides from sera of leukemia patients. This composite nanosheet greatly contributes to the MS analysis of phosphopeptides and gives inspiration in the pursuit of 2D structured materials for separation of other biological molecules of interests.

Received 28th November 2014,

Accepted 26th January 2015

DOI: 10.1039/c4nr07041k

www.rsc.org/nanoscale

Introduction

As a pioneering two-dimensional (2D) nanoarchitecture, graphene has gained sensational success in a wide range of applications during the past decade,^{1–3} thereby advancing efforts in further exploration of other analogues in the 2D material family. Subsequently, 2D transition metal dichalcogenides

(TMDs, such as MoS₂, WS₂, and TiSe₂)^{4–6} and charged 2D transition-metal oxide nanosheets⁷ have demonstrated their fascinating performance in optoelectronic devices,^{8,9} sensing platforms,^{10–12} energy conversion,¹³ photoconductors and photocatalysts.^{14–16} However, the flourish in aforementioned applications is not the complete offering endowed by the burgeoning field of 2D nanosheets, and many applications based on their unique crystal structures and morphology have yet to be exploited and understood. Amidst their large untapped potential, their possible application in high-efficiency biological separation due to their extremely large surface area is of great significance in the biomedical field but thus far virtually unimplemented.

By altering protein functions and activities, reversible protein phosphorylation regulates cellular growth, division, differentiation and signaling.¹⁷ Mass spectrometric methods have been considered to be the most powerful tool in comprehending such highly complicated processes,^{18,19} but are in effect troubled by the low abundance and stoichiometry of phosphorylation, which has severely limited the accurate global characterization of phosphopeptides/phosphoproteins. To tackle this issue, phosphopeptide enrichment strategies

State Key Laboratory of Analytical Chemistry for Life Science, School of Chemistry and Chemical Engineering, Nanjing University, Nanjing 210093, P. R. China.

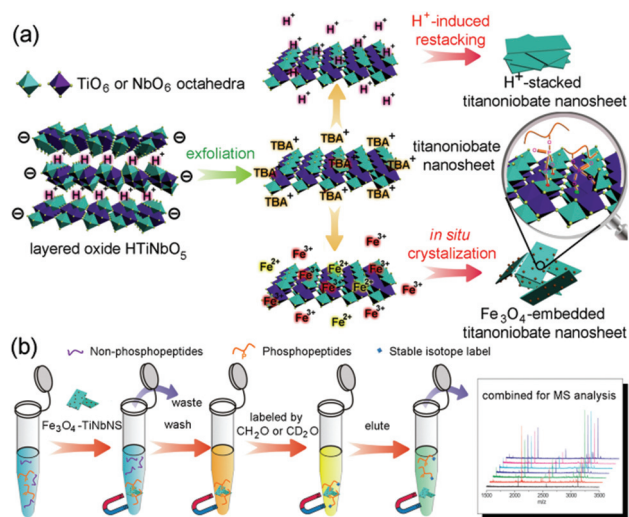
E-mail: minqianhao@nju.edu.cn; Fax: +86 25 83597204; Tel: +86 25 83597204

† Electronic supplementary information (ESI) available: Sequence of phosphopeptides from the digests of α - and β -casein; percentages of the 4 methylated products from peptide β 1 at different labeling reaction times; sequence of serum phosphopeptides; XPS spectra of Nb 3d and Ti 2p in layered oxides and H⁺-stacked nanosheets; phosphopeptide enrichment sensitivity of bulk oxides, layered oxides and H⁺-stacked nanosheets; AFM image of TiNbNS; saturated adsorption isotherm for pNPP adsorbed on bulk oxides, layered oxides and H⁺-stacked nanosheets; XPS spectra of Fe₃O₄-TiNbNS; nitrogen adsorption-desorption isotherms and pore size distribution curves for the Fe₃O₄ nanocrystals; phosphopeptide enrichment sensitivity, capacity and selectivity of the Fe₃O₄-TiNbNS composites; MS/MS spectra of phosphopeptides enriched from serum; linear relationship between the logarithms of peak area ratio and loading volume ratio. See DOI: 10.1039/c4nr07041k

were initially developed based on bioseparation materials in immobilized metal ion affinity chromatography (IMAC)²⁰ and metal oxide affinity chromatography (MOAC).^{21,22} In its nascent stage, the separation probes for phosphopeptides were mainly prepared in zero-dimensional structures such as nanoparticles or nanospheres of TiO_2 ,²¹ ZrO_2 ,²² or Al_2O_3 .²³ Although certain progress was made thereafter in improving magnetic controllability by incorporating the magnetic component Fe_3O_4 , the core performances were still far from satisfying the requirements of high capacity separation and sensitivity.^{24,25} Since then, macroporous,^{26,27} mesoporous,^{28,29} and even metal-organic frameworks (MOFs),³⁰ equipped with large surface areas and smooth mass transfer channels, as well as their core-shell nanostructured variants integrating Fe_3O_4 as the inner core to facilitate fast and efficient separation,^{31,32} have been elaborately designed to enhance the efficiency of enrichment while accelerating sample pretreatment. Very recently, along with the advent of 2D graphene-based materials, graphene or graphene oxide have been increasingly adopted as platforms to broaden the contact area for holding IMAC or MOAC probes, allowing easy access and adequate binding of guest phosphorylated biomolecules.^{33–35} However, the overall performance of graphene-based composites greatly depended on the actual coverage of affinity species (metal ions or metal oxides), and the uncovered graphene substrate made no contribution to binding phosphopeptides but left opportunities for non-specific adsorption, which had a negative influence on the selectivity. Thereby, it can be anticipated that a type of 2D material with adsorbability toward phosphate groups could be an excellent alternative to graphene-based composites.

This possibility may lie in a unique class of layered compounds termed cation-exchangeable layered transition metal oxides, which can be delaminated into negatively charged 2D nanosheets.^{36,37} Among them, titanate, niobate and titanoniobate nanosheets have demonstrated the remarkable photocatalytic and alcoholic activity of their abundant and strong Lewis acid sites,^{38–40} which are indeed the prerequisite for chemoaffinity towards phosphate groups. Their periodic structural units, TiO_6 and NbO_6 octahedra, shared with classical phosphopeptide affinity materials TiO_2 and Nb_2O_5 crystals, also provide the possibility of separating and enriching phosphopeptides.

Based on their crystalline similarity, we herein build a bridge connecting 2D nanomaterials to the arena of biological separation by introducing niobate and titanoniobate transition metal oxide nanosheets (NbNS and TiNbNS) into the family of phosphate affinity probes for recognizing and capturing phosphopeptides from a large excess of counterparts. Moreover, making use of the negative charge expressed on the polyanion nanosheets, Fe_3O_4 nanocrystals were *in situ* generated from preloaded precursor cations to form titanoniobate nanosheets embedded with Fe_3O_4 nanocrystals (Fe_3O_4 -TiNbNS), which were applied in qualitative and quantitative characterization of phosphopeptides *via* enrichment and *in situ* isotope labeling (Scheme 1). Due to the transformation in morphology from bulk to 2D state, titanoniobate nanosheets exposed more plentiful Lewis acid sites for accepting phosphate groups, most of



Scheme 1 Schematic illustration of (a) the synthetic procedure for the Fe_3O_4 -TiNbNS composite and (b) workflow for phosphopeptide capture and *in situ* isotope labeling based on Fe_3O_4 -TiNbNS.

which would have been inaccessible in the layered metal oxides. Not only serving as a magnetic medium to ease sample processing, Fe_3O_4 nanocrystals embedded on the surface could also disturb the restacking between nanosheets, maintaining adequate active surface and space for adsorption of phosphopeptides and allowing further on-site reactions. Thanks to the above advantages brought about by the 2D morphology and Fe_3O_4 nanocrystals, the Fe_3O_4 -TiNbNS composite possessed excellent sensitivity, selectivity and capacity in phosphopeptide enrichment as well as simplicity in sample processing, and allowed *in situ* isotope labeling in investigating the dysregulated phosphopeptides in sera of leukemia patients.

Experimental section

Preparation of NbNS and TiNbNS

KNb_3O_8 was prepared by grinding and then heating a stoichiometric mixture of Nb_2O_5 and K_2CO_3 at 900 °C for 10 h. Likewise, a mixture of K_2CO_3 , Nb_2O_5 , and TiO_2 in a stoichiometric ratio underwent a similar solid phase reaction at 1100 °C over 24 h to form layered KTiNbO_5 . Afterwards, the proton exchange reaction was performed by suspending 1 g of as-prepared KNb_3O_8 or KTiNbO_5 in a 5 M HNO_3 aqueous solution with stirring at room temperature for 3 days. After being rinsed by water three times, the layered oxides HNB_3O_8 and HTiNbO_5 were collected and heated at 60 °C until dry.

1 g of the layered oxide (HNB_3O_8 or HTiNbO_5) was dispersed in 100 mL of water and stirred while 10% tetrabutyl ammonium hydroxide (TBAH) was added dropwise until the pH value increased to 10. After continuous stirring for 7 days, the suspension was centrifuged at 9000 rpm for 10 min, and the supernatant containing NbNS or TiNbNS was collected for further use. To obtain the H^+ -stacked nanosheets, 100 mL of 1 mol L^{-1} HNO_3 aqueous solution was added dropwise into

100 mL of the NbNS or TiNbNS solution to induce formation of aggregates, which were then centrifuged and successively washed by ethanol and water three times to remove TBAH and HNO_3 . The concentrations of NbNS and TiNbNS were calculated to be 5.4 mg mL^{-1} and 9.4 mg mL^{-1} , respectively, by weighing the H^+ -stacked nanosheets after they were dried.

Preparation of Fe_3O_4 -TiNbNS

0.25 mol L^{-1} FeCl_3 was combined with 0.125 mol L^{-1} FeCl_2 aqueous solution in equal volume to form the Fe source solution, in which the resultant concentrations of Fe^{3+} and Fe^{2+} were respectively 0.125 mol L^{-1} and $0.0625 \text{ mol L}^{-1}$. Nitrogen was bubbled into the stock solutions of the nanosheets and the Fe source in advance to remove dissolved oxygen. Afterwards, the TiNbNS solution was diluted with 15 mL of deionized water, and a certain volume of the Fe source solution was added dropwise with mechanical stirring. After stirring for another 10 min, 25 mL of 2 mol L^{-1} $\text{NH}_3 \cdot \text{H}_2\text{O}$ was introduced drop-by-drop to create a basic condition for the co-precipitation of Fe^{3+} and Fe^{2+} . The obtained Fe_3O_4 -TiNbNS composite was isolated from the supernatant, rinsed with ethanol and water three times with the help of a magnet, and finally dispersed in water for use. As a control, pure Fe_3O_4 nanoparticles were generated *via* the above co-precipitation procedure in the absence of the TiNbNS colloids.

Capture of phosphopeptides

Digests for phosphopeptide capture were diluted to certain concentrations with a loading buffer containing 6% (v/v) TFA and 50% (v/v) ACN. 0.1 mg of the affinity material was dispersed into a 200 μL sample solution, and vibrated in a vortex for 30 min. After the supernatant was removed by centrifugation at $12\,000g$ for 3 min (layered materials, H^+ -stacked nanosheets) or magnetic separation (Fe_3O_4 -TiNbNS composites), the affinity material combined with the phosphopeptides was rinsed twice with 200 μL of 0.1% (v/v) TFA 50% (v/v) ACN containing 200 mM NaCl and then 200 μL of 0.1% (v/v) TFA 50% (v/v) ACN, respectively. Afterwards, 10 μL of 10% $\text{NH}_3 \cdot \text{H}_2\text{O}$ was introduced to elute the captured phosphopeptides from the affinity materials under sonication for 15 min.

In situ isotope dimethyl labeling of phosphopeptides

In situ isotope labeling was performed right after phosphopeptide capturing and non-phosphopeptide rinsing steps and before the elution step demonstrated above. At that point, the affinity material was dispersed into 200 μL of 100 mM sodium acetate buffer (pH = 5.8), followed by the addition of 8 μL of 4% (v/v) CH_2O or CD_2O and 8 μL of 0.6 M NaBH_3CN . After vibration in a vortex for 40 min, the labeling reaction was terminated by the addition of 10 μL of 88% formic acid (FA). Further rinsing with 200 μL of 0.1% (v/v) TFA solution in 50% (v/v) ACN was required to remove excess labeling reagents. Lastly, phosphopeptides enriched on the affinity materials and labeled *in situ* by CH_2O or CD_2O were harvested by adding 10 μL of 10% $\text{NH}_3 \cdot \text{H}_2\text{O}$.

Relative quantification of serum phosphopeptides

Human serum samples were collected from 8 healthy adults and 8 patients with acute promyelocytic leukemia in Nanjing Drum Tower Hospital according to their standard clinical procedures. The control sample was the mixture of sera from 20 healthy volunteers in Nanjing University Hospital. All the human serum samples were collected with consent of both patients and healthy volunteers, and the use of human serum samples were performed in compliance with the relevant laws and institutional guidelines. Also, we have obtained the ethical approval of the protocols from the institutional committee. Typically, 8 μL of raw serum was diluted to 200 μL by loading a buffer containing 0.5% TFA and shaken with 0.1 mg of Fe_3O_4 -TiNbNS for 30 min. Afterwards, the phosphopeptide capturing, labeling, rinsing and eluting procedures were the same as in the above experiments. For relative quantification, 0.5 μL aliquots were pipetted from the eluents for healthy adults/patients (light-labeled) and the control sample (heavy-labeled), combined and deposited onto the MALDI target.

Results and discussion

Morphologies and structures of NbNS and TiNbNS

For screening the nanosheet of optimal phosphopeptide affinity, both titanoniobate and niobate were initially investigated as phosphate absorbents. Layered metal oxides HfNb_3O_8 and HTiNbO_5 were obtained through proton exchange reaction from their potassium salts KNb_3O_8 and KTiNbO_5 , and delaminated into isolated niobate/titanoniobate nanosheets (NbNS/TiNbNS). After collection of the NbNS/TiNbNS colloids, H^+ was reintroduced to induce aggregation of the nanosheets. The morphologies of layered oxides HfNb_3O_8 and HTiNbO_5 as well as their H^+ -stacked nanosheets were characterized by scanning electron microscopy (SEM) and transmission electron microscopy (TEM). As shown in Fig. 1a and b, HfNb_3O_8 and HTiNbO_5 exhibited a wafer biscuit-like morphology, with numerous highly ordered plates tightly assembled together. After exfoliation and regeneration by H^+ -induced stacking, SEM images displayed a film featuring disordered wrinkles, indicating the overall 2D morphology of the nanosheets (Fig. 1c). From the viewpoint of TEM (Fig. 1d), exfoliated HfNb_3O_8 and HTiNbO_5 nanosheets sized at about 300 nm were aggregated in a random manner, providing a larger accessible surface for guest molecules in biological separation than their parent layered oxides. Under the magnification of high-resolution TEM (HRTEM), the lattice fringe was clarified in the few-layer domain for both the HfNb_3O_8 and HTiNbO_5 nanosheets (Fig. 1e). As is evident from the selected-area electron diffraction (SAED) patterns of the single sheet (Fig. 1e insets), the bright orthorhombic lattice of the 2D sheets further confirmed the inheritance from the original crystal structures of the layered oxides HfNb_3O_8 and HTiNbO_5 . As characterized by X-ray diffraction (XRD) (Fig. 2), the diffraction peaks of layered oxides HfNb_3O_8 and HTiNbO_5 matched well with the JCPDS card no. 44-0672 and 75-2062. The sharp dominant peaks

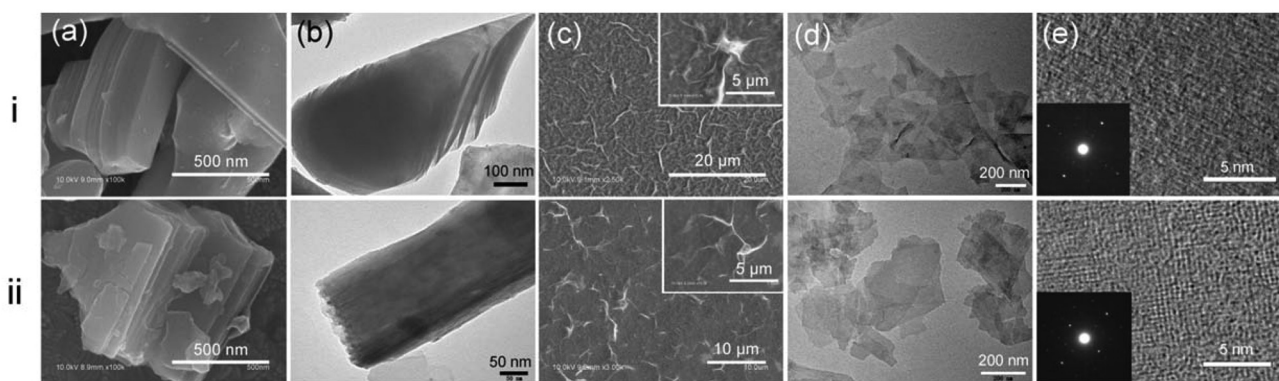


Fig. 1 (a–e) SEM and TEM images of layered oxides HNb_3O_8 and HTiNbO_5 as well as the H^+ -stacked nanosheets: (a and b) images of layered oxides; (c and d) images of H^+ -stacked nanosheets; (e) HRTEM of few-layer nanosheets with SAED patterns shown in the insets. Row (i) and (ii) correspond respectively to HNb_3O_8 and HTiNbO_5 .

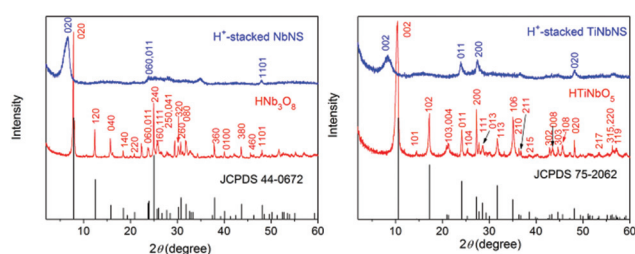


Fig. 2 XRD patterns for HNb_3O_8 and HTiNbO_5 as well as for the H^+ -stacked nanosheets corresponding to JCPDS 44-0672 and 75-2062.

respectively assigned to the 020 plane of HNb_3O_8 and the 002 plane of HTiNbO_5 indicated the well-ordered structure of both layered oxides, and the layer distances were calculated to be 1.12 nm and 0.83 nm, respectively. For H^+ -stacked samples of both HNb_3O_8 and HTiNbO_5 , in addition to the smaller number of diffraction peaks, the peaks designated to the 020 plane of HNb_3O_8 and the 002 plane of HTiNbO_5 were markedly weakened and shifted to the low angle region, evidencing the poorer periodic structure of the stacked nanosheets than the layered oxides. The chemical environment of surface Nb and Ti in the layered oxides and nanosheets was identified by X-ray photoelectron spectroscopy (XPS). As displayed in Fig. S1a,† the Nb $3d_{5/2}$ and $3d_{3/2}$ peaks of HNb_3O_8 are located at 207.2 eV and 210.0 eV, basically identical to the Nb 3d spectrum of bulk

Nb_2O_5 (207.3 eV and 210.1 eV).⁴¹ Meanwhile, the Nb 3d peaks of layered HTiNbO_5 are centered around a similar region (Fig. S1b†), and the binding energy of the Ti 2p agreed well with the reported value of octahedral-coordinated Ti(IV) in TiO_2 crystals (Fig. S1c†).⁴² Furthermore, the peak positions of both the Nb 3d and Ti 2p in layered oxides HNb_3O_8 and HTiNbO_5 remained constant even after exfoliation and H^+ -induced stacking. These observations gave solid evidence for the fact that the chemical environment of the metal ion in HNb_3O_8 and HTiNbO_5 as well as in NbNS and TiNbNS coincided with those of conventional MOAC materials TiO_2 and Nb_2O_5 at the highest valence, proving the theoretical feasibility of capturing phosphopeptides in a mechanism similar to TiO_2 and Nb_2O_5 .

Layered oxides HNb_3O_8 , HTiNbO_5 and their H^+ -stacked nanosheets were utilized in the capture of phosphopeptides from tryptic digests of β -casein (1.6 pmol), a standard phosphoprotein, in comparison with commercial Nb_2O_5 and TiO_2 . Fig. 3 summarizes the MALDI-TOF MS spectra of the phosphopeptides enriched by the six types of affinity materials, with detailed information of the captured phosphopeptides listed in Table S1.† Classical phosphate affinity probes TiO_2 and Nb_2O_5 were only rarely able to capture and regenerate 3 phosphopeptides, whose signals came out of relatively rough base-lines in the MS spectra (Fig. 3a and b). Using layered HNb_3O_8 and HTiNbO_5 , the MS detector showed signals for 4 phosphopeptides, with enhanced peak intensity and better S/N ratio

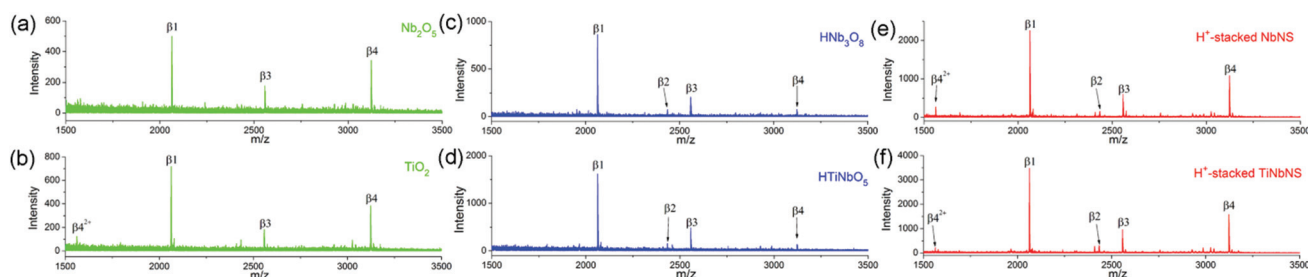


Fig. 3 MALDI-TOF MS spectra of tryptic digests of β -casein (1.6 pmol) enriched by (a) Nb_2O_5 , (b) TiO_2 , (c) HNb_3O_8 , (d) HTiNbO_5 , (e) H^+ -stacked NbNS, and (f) H^+ -stacked TiNbNS.

(Fig. 3c and d). Also note that the signal for multi-phosphopeptide $\beta 4$ underwent a decline in contrast with the dramatically intensified peak of monophosphopeptide $\beta 1$. This bias can be explained by the different surface characteristics in that the exposed surface on the layered oxide is mainly a unique crystal face (020 and 002 for HfNb_3O_8 and HTiNbO_5 , respectively) due to exceptionally high 2D anisotropy, while diverse surface crystal planes may have the same chance to occupy the surface sites of regular oxide crystals due to their isotropic structure. In this sense, the surface five-coordinated Ti or Nb species on the unique crystal face may preferentially bind to the monophosphopeptides in a bridging bidentate fashion.^{27,43} Upon further morphological conversion from layered structures to nanosheets, the H^+ -stacked nanosheets exhibited more efficient and less discriminative enrichment, producing 4 signature peaks with enhanced intensities in both spectra (Fig. 3e and f). This improved sensitivity and unbiased enrichment was attributed to the enlarged active surface after exfoliation into 2D nanosheets, which provided abundant Lewis acid sites and a spacious microenvironment for effective phosphopeptide enrichment and unimpeded elution. The enrichment of sensitivity by these Ti/Nb-based materials was also investigated. At a loading of 160 fmol, signals derived from phosphopeptides were fairly low or even undetectable using the bulk (Nb_2O_5 and TiO_2) and layered oxides (HfNb_3O_8 and HTiNbO_5) (Fig. S2†). In contrast, the H^+ -stacked nanosheets still allowed distinct detection of phosphopeptides, and the strongest signal and best S/N ratio was given by H^+ -stacked TiNbNS . Further reduction of the loading led to no MS peak in the spectra except for H^+ -stacked TiNbNS , which reached a limit of detection of 40 fmol for β -casein and generated 3 peaks assigned to phosphopeptides (Fig. S3†). Overall, varying with morphology, the performance of 2D nanosheets in capturing phosphopeptides was significantly improved in comparison with their homologous bulk and layered metal oxides, and TiNbNS was selected as the better block from which to build composite architectures.

Morphology and properties of Fe_3O_4 - TiNbNS

Having determined the optimal candidate to be the affinity probe for capturing phosphopeptides, we next sought to combine magnetic manipulation with biological separation by interfacing Fe_3O_4 nanocrystals with TiNbNS to produce a composite nanosheet. As the structural unit of Fe_3O_4 - TiNbNS , TiNbNS was further characterized by atomic force microscopy (AFM) to profile its 2D structure. According to the image and height analysis in Fig. S4,† TiNbNS was determined to have a fully exfoliated 2D nanostructure with a thickness of 1 nm. Rather than feeding H^+ into the nanosheet colloids to induce restacking, we treated Fe^{2+} and Fe^{3+} as the initiating ions for precipitating negatively charged TiNbNS . Moreover, the immobilized Fe^{2+} and Fe^{3+} could also serve as precursors of Fe_3O_4 nanocrystals at the high pH value caused by $\text{NH}_3\cdot\text{H}_2\text{O}$. During the construction of the composite, the dosage of the Fe source was a pivotal factor in the growth of the Fe_3O_4 nanocrystals and the morphology of the composite. Fig. 4 displays the

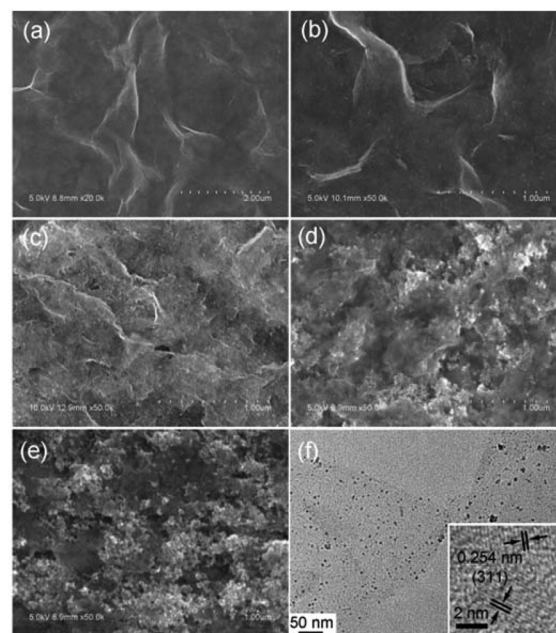


Fig. 4 (a–e) SEM images of Fe_3O_4 - TiNbNS prepared with Fe source to TiNbNS solution volume ratio of (a) 1 : 6, (b) 2 : 6, (c) 4 : 6, (d) 4 : 3 and (e) 6 : 3. (f) TEM image of Fe_3O_4 - TiNbNS -4-6. The inset in (f) shows the lattice distance of a Fe_3O_4 crystal, assigned to its 311 crystal face.

SEM and HRTEM images of the titanoniobate nanosheets embedded with Fe_3O_4 nanocrystals, denoted as Fe_3O_4 - TiNbNS - x - y , where x and y are, respectively, the volumes in mL of the Fe source and TiNbNS solutions. By introducing a relatively small amount of the Fe source (1 : 6), nanoparticles could hardly be seen in the image of the nanosheet (Fig. 4a). Upon addition of more Fe source (2 : 6), tiny nanoparticles of ca. 7 nm were generated and loosely distributed on the 2D nanosheet (Fig. 4b). In both of the above cases, the majority of the Fe^{3+} and Fe^{2+} ions were immobilized on negative charges in advance, leaving few ions in solution for seed formation and crystal growth, which accounted for their quite weak magnetic response and prolonged magnetic separation time. When the volume ratio increased to 4 : 6, uniformly arranged nanocrystals sized between 5 and 8 nm were spread all over the nanosheets (Fig. 4c and f), with only a few larger particles which were inferred to be the product of in-solution $\text{Fe}^{3+}/\text{Fe}^{2+}$ coprecipitation. Displayed in Fig. 4d and e is serious aggregation of Fe_3O_4 nanocrystals, which was yielded by the enormous excess of $\text{Fe}^{3+}/\text{Fe}^{2+}$ in solution and adsorbed onto the nanosheets afterwards. Depending on the variation in morphology with different feeding ratios, the whole process of *in situ* growth of Fe_3O_4 nanocrystals on the 2D nanosheets could be hypothesized as being two steps: first, the initially introduced $\text{Fe}^{3+}/\text{Fe}^{2+}$ cations were electrostatically attracted onto the electronegative surface of TiNbNS , with the rest of the $\text{Fe}^{3+}/\text{Fe}^{2+}$ cations freely dispersed in the surroundings; along with the increase in pH value, $\text{Fe}^{3+}/\text{Fe}^{2+}$ cations around $\text{Fe}^{3+}/\text{Fe}^{2+}$ - TiNbNS aggregates might react with pre-adsorbed ones at their sites on the nanosheets to produce crystal seeds. The likeli-

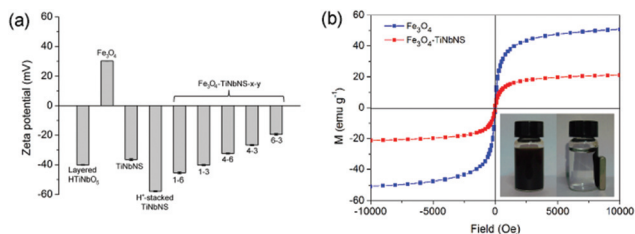


Fig. 5 (a) Zeta potential values for layered HTiNbO₅, Fe₃O₄, TiNbNS, H⁺-stacked TiNbNS, and Fe₃O₄-TiNbNS-x-y with different precursor ratios. (b) Magnetic hysteresis curves for Fe₃O₄ and Fe₃O₄-TiNbNS-4-6 examined at 300 K; the inset displays the magnetic separability of Fe₃O₄-TiNbNS in the presence of an external magnet.

hood of co-precipitation between in-solution Fe³⁺/Fe²⁺ cations also needed to be taken into account, especially in the case where Fe³⁺/Fe²⁺ cations are in excess.

Zeta potential measurement was performed to monitor the exfoliation of layered HTiNbO₅ and formation of TiNbNS embedded with magnetite particles (Fig. 5a). After TBA⁺-induced exfoliation, TBA⁺ ions adsorbed on electronegative TiNbNS comprised the stationary layer, which was surrounded by a diffusion layer of mobile counter ions,⁴⁴ and therefore slightly weakened the electronegativity from -40.1 to -36.5 mV. Upon introduction of H⁺, the double layer was reestablished by cation exchange between H⁺ and TBA⁺, and the zeta potential was measured to be more negative at -57.8 mV. Colloids with higher zeta potential (negative or positive) were more electrically stable in suspension due to electrostatic repulsion,⁴⁵ but in our case the addition of H⁺ disturbed the stability of the nanosheet dispersion and resulted in irreversible precipitates. The precipitation was actually caused by the enlarged size of the colloidal particles, implying that restacking of TiNbNS occurred in solution. Once the Fe₃O₄ nanocrystals were generated, the overall zeta potential (negative) was positively shifted and experienced a stepwise decline with an increase of Fe source, as a result of the accumulated Fe₃O₄ component in the composite. The magnetic property of the Fe₃O₄-TiNbNS composite was demonstrated using a superconducting quantum interference device (SQUID) at 300 K (Fig. 5b). Typically, the saturation magnetization value of Fe₃O₄-TiNbNS-4-6 was 21.1 emu g⁻¹, which enabled a quick separation within 20 s by placing a magnet next to the solution (Fig. 5b inset). The content of Fe₃O₄ in the composite was estimated to be 49.6% through quantifying the Fe present by inductively coupled plasma atomic emission spectroscopy (ICP-AES). Through calculation, the theoretical saturation magnetization value for the Fe₃O₄ component should be 42.5 emu g⁻¹, lower than the measured value (50.8 emu g⁻¹) of the pure Fe₃O₄ nanoparticles prepared in the absence of TiNbNS. This magnetism discrepancy offered additional evidence that the *in situ* nucleation and growth gave rise to Fe₃O₄ nanocrystals with different character from those obtained by the in-solution strategy.

For better understanding of the intrinsic phosphate adsorbability of Fe₃O₄-TiNbNS, a small molecule containing a phos-

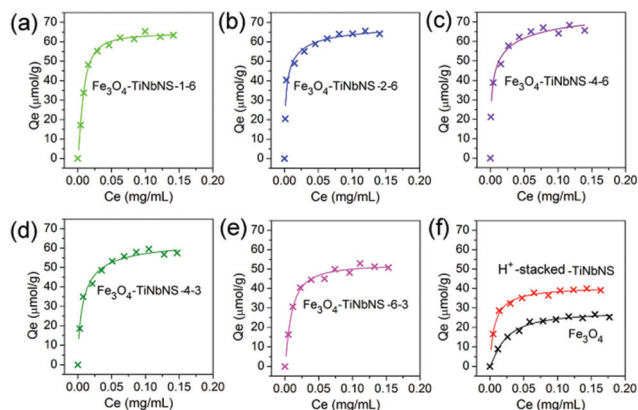


Fig. 6 Saturated adsorption isotherms for pNPP adsorbed on (a–e) Fe₃O₄-TiNbNS-x-y composites, (f) Fe₃O₄ and H⁺-stacked TiNbNS. Ce: equilibrium concentration; Qe: amount adsorbed at equilibrium.

phate group, *p*-nitrophenylphosphate (pNPP), was employed as the target molecule for plotting the saturated adsorption curves. As depicted in Fig. S5,† the saturated loading of phosphate on H⁺-stacked TiNbNS was measured to be around 40 μmol g⁻¹, the highest among the six Ti/Nb-based materials, exhibiting the most Lewis acid sites exposed for binding pNPP. Comparing the Fe₃O₄-TiNbNS composite with H⁺-stacked TiNbNS, we found that coupling Fe₃O₄ nanocrystals onto the nanosheets was able to considerably enhance the adsorption capacity up to 65 μmol g⁻¹ (Fig. 6). As Fe₃O₄ itself exhibits only relatively low adsorption of pNPP, the extraordinary improvement in phosphate affinity should not be mostly attributed to the relatively weak Lewis acidity of the Fe₃O₄ components,⁴⁶ as is also implied by the slightly decreased adsorption on Fe₃O₄-TiNbNS-6-3, the carrier of the most Fe₃O₄ nanocrystals.

Next arose the question of why the Fe₃O₄-TiNbNS composite afforded even higher phosphate loading than unmodified TiNbNS aggregates, and urged us to investigate the nature of the surface and variation in morphology triggered by additional Fe₃O₄ nanocrystals. The XPS survey spectrum shows the co-existence of Fe, O, Ti and Nb (Fig. S6a†). The binding energy values of the Nb 3d and Ti 2p (Fig. S6b and c†) coincide well with those obtained from layered oxide HTiNbO₅ and H⁺-stacked TiNbNS, confirming the preservation of the chemical environment of surface Ti and Nb even during the formation of the Fe₃O₄ nanocrystals. The information on porosity and specific surface area was obtained from the nitrogen adsorption-desorption curves (Fig. 7a). Unexfoliated HTiNbO₅ showed a type II isotherm, indicative of a typical non-porous or macroporous adsorbent, which was also rationalized by its extremely low BET surface area (4.7 m² g⁻¹). The isotherms of both post-exfoliation products, H⁺-stacked TiNbNS and Fe₃O₄-TiNbNS-4-6 were type IV with a visible hysteresis loop classified as type H3, assigned to slit-shaped pores produced by the aggregation of plate-like nanostructures.⁴⁷ In addition, a minor expansion in surface area (38.5 m² g⁻¹) was observed after the exfoliation process, but restacking between

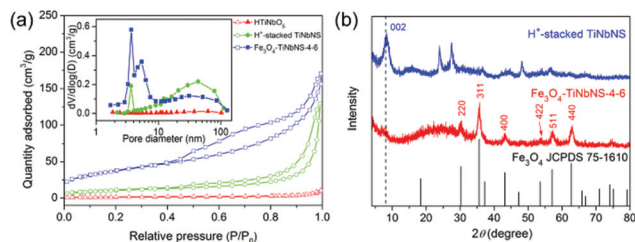


Fig. 7 (a) Nitrogen adsorption-desorption isotherms and pore size distribution curves (inset) calculated from the desorption branches of HTiNbO₅, H⁺-stacked TiNbNS, and Fe₃O₄-TiNbNS-4-6. (b) XRD pattern for Fe₃O₄-TiNbNS-4-6 matched with magnetite JCPDS 75-1610.

nanosheets counteracted the enhancement. On the other hand, *in situ* growth of Fe₃O₄ could maintain the space between adjacent nanosheets and thus compromise the restacking to some extent, leading to a dramatically enlarged surface area (135.5 m² g⁻¹). Demonstrated in the pore size distribution curves (Fig. 7a inset), the dominant pore size distribution peaks for Fe₃O₄-TiNbNS and H⁺-stacked TiNbNS were both located at 3.7 nm, corresponding to the slits between restacked layers. Notably, a shoulder peak centered at 5.4 nm was detected exclusively for Fe₃O₄-TiNbNS, which was speculated to come from the gaps inside the incompact stack caused by the extrinsic Fe₃O₄ species. In this manner, the additional surface and space newly exploited by the Fe₃O₄ nanocrystals released extra Lewis acid sites for accommodating more phosphate, which could elucidate the underlying principle as to why the Fe₃O₄-TiNbNS composite possessed higher capacity than H⁺-stacked TiNbNS in phosphate adsorption. The nitrogen adsorption-desorption curve for pure Fe₃O₄ nanocrystals gave a starkly different pattern (Fig. S7†), and the pore diameter (8.8 nm) of the agglomerates was larger than the secondary pore size of the Fe₃O₄-TiNbNS composite. Supported by this characterization, we can infer with more confidence that Fe₃O₄ nanocrystals were generated *in situ* on nanosheets along a pathway rather distinct from in-solution crystallization. In the representative XRD pattern (Fig. 7b), a set of diffraction peaks matching well with the theoretical pattern of magnetite Fe₃O₄ (JCPDS 75-1610), and the approximate particle size calculated using the Debye-Scherrer equation was 7.8 nm, close to the diameter measured from the SEM and TEM images (Fig. 4c and f). Even more noteworthy was that the 002 face diffraction peak was significantly weaker than that of H⁺-stacked TiNbNS, reflecting that the regularity of the restacked structure received further perturbation upon doping with Fe₃O₄ nanocrystals. It can be speculated that instead of the restacking effect induced by H⁺, the embedded Fe₃O₄ obstacles loosened the interaction between the nanosheets and diminished the recovery of the stacked nanostructure. From the structural interpretation by XRD, we could reach an identical conclusion to the nitrogen adsorption-desorption measurements that the Fe₃O₄ component played a crucial part in enhancing the total surface area and providing extra space for the adsorption events occurring on the nanosheet surface.

Selective capture and isotope labeling of phosphopeptides

Encouraged by the enhanced surface area and porosity, we were eager to see if the newly constructed Fe₃O₄-TiNbNS could lead to an improvement in capturing phosphopeptides. Fig. 8 shows the MALDI-TOF MS spectra of tryptic digests of β-casein (1.6 pmol) after enrichment with Fe₃O₄-TiNbNS composites. As illustrated in Fig. 8a and b, the MS peaks for the phosphopeptides captured by Fe₃O₄ nanocrystals had about one-fifth of the intensity of those obtained from the TiNbNS series, indicating that TiNbNS was still the major force in the Fe₃O₄-TiNbNS composite contributing to the adsorption of phosphopeptides. The group of Fe₃O₄-TiNbNS composites exhibited similar signal intensity to H⁺-stacked TiNbNS in the detection of monophosphopeptides β1, β2, and β3, but witnessed a 3-fold elevation in the enrichment abundance of tetraphosphopeptide β4 (Fig. 8c-g). The similar enhancement specifically for multi-phosphopeptides also occurred by comparing the layered oxides with H⁺-stacked nanosheets (Fig. 3c-f). Meanwhile, the performance of Fe₃O₄-TiNbNS composites on enriching phosphopeptides did not dramatically vary with the precursor ratios, except in the modest decline of the multi-phosphorylated species β4 when a higher proportion of Fe₃O₄ was introduced (Fig. 8f and g). This minor deterioration of phosphate affinity was probably due to the decreased relative content of TiNbNS. In the sensitivity evaluation, 4 distinct analyte peaks with a higher signal-to-noise ratio were identified from 160 fmol digests of β-casein after enrichment with the Fe₃O₄-TiNbNS series (Fig. S8†). For the further lowered loading (16 fmol), signals of phosphopeptides β1, β2, and β3 were still detectable for Fe₃O₄-TiNbNS at every ratio (Fig. S9†), whilst the H⁺-stacked TiNbNS could only give a detection limit of 40 fmol (Fig. S3†). This sensitivity is much better than the TiO₂ or ZrO₂ coated magnetic probes,^{25,48} and comparable with the mesoporous TiO₂ nanostructures.^{31,49} In comparison with 2D graphene-supported separation materials presented in previous studies,^{33,34,50} Fe₃O₄-TiNbNS also exhibits higher detection sensitivity towards both mono- and multi-phosphopeptides. In line with the better performance in adsorption of

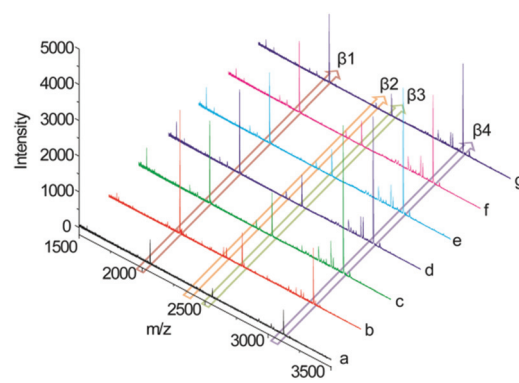


Fig. 8 MALDI-TOF MS spectra of tryptic digests of β-casein (1.6 pmol) enriched by (a) Fe₃O₄, (b) H⁺-stacked TiNbNS, and (c-g) Fe₃O₄-TiNbNS-x-y (c-g is successively assigned to 1 : 6, 2 : 6, 4 : 6, 4 : 3, and 6 : 3).

pNPP, participation of Fe_3O_4 nanocrystals in the nanosheets made a similar contribution to the further improved sensitivity in phosphopeptide enrichment, which we attribute to the hampered TiNbNS restacking process and larger active surface preserved by the Fe_3O_4 nanocrystals generated *in situ*. Considering the degraded enrichment efficiency at high precursor ratios (4 : 3 and 6 : 3) as well as the weak magnetism due to the low Fe_3O_4 percentage (1 : 6 and 2 : 6), we eventually determined Fe_3O_4 - TiNbNS -4-6 to be the optimal composite for further evaluation and extended application.

To assess the selectivity of the Fe_3O_4 - TiNbNS composite in trapping phosphopeptides, tryptic digests of bovine serum albumin (BSA) were employed as interference to create a more complex environment. Fig. S10a† shows that once 10-fold digests of BSA were introduced, the signals of the phosphopeptides coming from β -casein (160 fmol) were totally overwhelmed by the massive peaks of the peptides degraded from BSA. After treatment with the Fe_3O_4 - TiNbNS composite, 4 phosphopeptides were recovered out of the clean background (Fig. S10b†), while layered oxide HTiNbO_5 was not capable of extracting the phosphorylated minority from the mixture (Fig. S10c†). Even when the mass ratio of BSA to β -casein was increased to 100 : 1, the Fe_3O_4 - TiNbNS composite still exhibited its excellent anti-interference ability by selectively adsorbing phosphopeptides from the non-phosphopeptide mixture (Fig. S10d and e†), but not even a scant signal of phosphopeptides could be observed using layered oxide HTiNbO_5 (Fig. S10f†). The enrichment capacity was evaluated by utilizing tryptic digests of α -casein (1.6 pmol), a standard phosphoprotein where around 20 amino acids were phosphorylated in total, as the test specimen. 18 phosphopeptides with various abundance and phosphorylation sites were successfully extracted by Fe_3O_4 - TiNbNS and yielded a group of peaks in the spectrum (Fig. S11a and Table S2†), suggesting that Fe_3O_4 - TiNbNS was equipped with the capability to co-enrich a large variety of phosphopeptides with diverse phosphorylation degree and abundance. On the contrary, only 10 phosphopeptides appeared in the product after pretreatment with layered oxide HTiNbO_5 (Fig. S11b†). The superior performance of the Fe_3O_4 - TiNbNS composite over layered oxide HTiNbO_5 both in enrichment selectivity and capacity was attributed to the expanded specific surface caused by exfoliation and extra active binding sites resulting from the disturbed restacking process by on-sheet Fe_3O_4 nanocrystals.

Stable isotope dimethyl labeling is a reliable and cost-effective strategy for quantitative proteomics, in which the N-terminus and ϵ -amino group of lysine go through reductive amination with formaldehyde (CH_2O) or deuterated formaldehyde (CD_2O) to cause a mass difference of 28 or 32 Da.⁵¹ In this work, we explored the potential of the Fe_3O_4 - TiNbNS composite as the carrier of as-captured phosphopeptides for *in situ* stable isotope dimethyl labeling. The process of *in situ* dimethyl labeling was monitored by quantifying the labeling products of phosphopeptide $\beta 1$ enriched from tryptic digests of β -casein (1.6 pmol). Peptide $\beta 1$ was estimated to take a longer time than other phosphopeptides to complete the

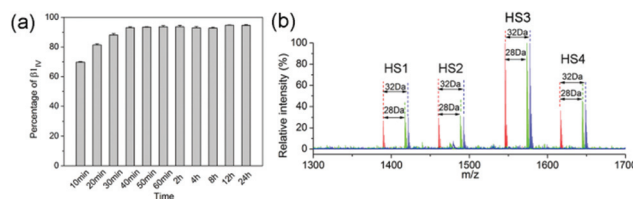


Fig. 9 (a) Percentage of fully labeled $\beta 1$ varying with reaction time. (b) Representative MALDI-TOF MS spectra of serum phosphopeptides enriched by the Fe_3O_4 - TiNbNS composite (red color) and labeled *in situ* by CH_2O (green color) and CD_2O (blue color).

labeling reaction, because it includes an extra lysine residue, which is also active for amination with formaldehyde. As shown in Fig. S12,† after reaction with the labeling reagent for 10 min, peptide $\beta 1$ gave no signal at the pristine position ($m/z \sim 2062$), but differentiated into 4 types of methylated products with different labeling extents (mono-, di-, tri- and tetra-methylated $\beta 1$, respectively denoted as $\beta 1_I$, $\beta 1_{II}$, $\beta 1_{III}$ and $\beta 1_{IV}$). With the continuing reaction, the peaks corresponding to incompletely labeled by-products were gradually weakened (Table S3†). By 40 min, the yield of $\beta 1_{IV}$ remained stable at around 94% for even a prolonged reaction time (Fig. 9a), which meant the labeling reaction reached thermodynamic equilibrium after 40 min. Due to the lesser degree of freedom, it was reasonable that peptides immobilized on the solid phase would experience a decelerated labeling reaction compared to that reported for the in-solution strategy.⁵¹

Relative quantification of serum phosphopeptides

As the most accessible bodily fluid sample, human serum is regarded as a library of masses of informative biomolecules such as proteins, peptides and microRNAs, whose dysregulated expressions are potentially associated with the occurrence and development of various diseases, including cancers.^{52,53} Endogenous phosphopeptides in serum have been extensively reported to serve as a reflective factor of many diseases, and the difference in expression is modulated by a cascade of endogenous proteases, whose activities are highly distinct between healthy and diseased states.⁵⁴ For relative quantification of serum phosphopeptides from normal and diseased specimens, an *in situ* isotope dimethyl labeling protocol was implemented after pre-enrichment based on the Fe_3O_4 - TiNbNS composite. As depicted in Fig. 9b, 4 endogenous phosphopeptides degraded from phosphorylated fibrinogen were enriched from a mixed serum of 20 healthy volunteers and fully labeled by CH_2O and CD_2O without any by-products, in accordance with the mass shift of 28 and 32 Da (MS/MS spectra and peptide sequences are listed in Fig. S13 and Table S4†). To demonstrate the reliability of *in situ* labeling for quantitative characterization of phosphopeptides, the isotope cluster area of the most intensive peak from phosphopeptide HS3 was recorded to plot a calibration curve by changing the loading of the light-labeled sample while keeping the heavy-labeled one constant. The peak area ratio changed proportionally

with loading volume ratio over the range from 8 : 1 to 0.125 : 1 (Fig. S14a†), and linear fitting provided an equation with slope and linear correlation coefficients of 0.966 and 0.996 (Fig. S14b†), validating the credibility of relative quantification in this range. So far, abnormal expression of serum fibrinogen and its phosphorylated fragments has been discovered and discussed in the cases of ovarian cancer,⁵⁵ gastric cancer⁵⁶ and liver cancer.²⁸ Unlike solid cancer tumors, leukemia is a group of hematologic malignancies featured by a large number of abnormal white blood cells, toward which phosphoproteomic research was extensively carried out regarding its complicated subtypes.^{57,58} To date, most of this endeavor has been directed to the exploration of the phosphoproteome in leukemia cell lines, with the goal of comprehending the signaling pathways of the tyrosine kinase family (Bcr-Abl kinase and Janus families) and assessing inhibitor drug (imatinib, dasatinib and nilotinib) efficacy,^{59,60} but the endogenous phosphopeptides existing in leukemia serum specimens were not as investigated or involved in the elucidation of pathology. Herein, taking the sera of leukemia patients as a research object, we applied an *in situ* labeling strategy based on Fe₃O₄-TiNbNS to characterize the levels of serum phosphopeptides. Serum samples were collected from 8 healthy adults and 8 patients with acute promyelocytic leukemia (APL), enriched by Fe₃O₄-TiNbNS-4-6 and labeled *in situ* with CH₂O, while mixed serum from 20 healthy volunteers was labeled with CD₂O as a control. All of the normalized MS spectra and relative abundance of captured phosphopeptides from the sera of healthy adults and leukemia patients (light-labeled) combined with the control sample (heavy-labeled) are illustrated in Fig. 10a and b by setting the value of the control sample as 100%. As presented in the bar chart (Fig. 10c and d), little difference was observed for all of the 4 phosphopeptides from the comparison between normal sera and the control group, whilst 3 of the 4 phosphopeptides in the sera drawn from leukemia patients

saw a significant variation compared to the control sample. As calculated from the logarithmic ratios of the isotope cluster areas, the phosphopeptide HS1 (D[pS]GEGDFLAEGGGV) and HS2 (AD[pS]GEGDFLAEGGGV) respectively underwent a 3.3 and 1.5-fold up-regulation, but the phosphopeptide HS4 (AD[pS]GEGDFLAEGGGVR) conversely turned out to be down-regulated by about 2.6 times. The elevation of phosphopeptide HS1 accompanied with the decline in phosphopeptide HS4 was also observed in profiling the serum phosphopeptides of patients with ovarian cancer or hepatocellular carcinoma.^{61,62} As for gastric cancer, down-regulation occurred on phosphopeptides HS2 and HS3, and yet expression of phosphopeptide HS4 was exceptionally raised.⁵⁶ It is also worth mentioning that the standard deviation of phosphopeptides HS1, HS2 and HS4 from leukemia patients was much higher than that from healthy adults, which can be explained by the highly complicated causes of the disease and variation of states across individuals compared to the relative centralized phenotype in normal specimens. It was extensively documented that APL always occurs in concomitance with disseminated intravascular coagulation (DIC), a disorder in blood coagulation accounting for the bleeding and thrombosis.⁶³ In these cases, fibrinopeptide A (FPA), the nonphosphorylated form of HS4, released from thrombin-induced degradation of fibrinogen during blood coagulation, was measured to be markedly elevated, reflecting the unexpected consumption of fibrinogen and the aberrant enzyme cascade.⁶⁴ To complicate matters further, a number of enzymes including kinases, alkaline phosphatases and amino-peptidases are all implicated in the generation of phosphorylated and truncated forms of FPA before or after thrombin action, resulting in the four endogenous phosphopeptides recovered in our study.⁶⁵ Taken together, the dissimilar profile of serum phosphopeptides to that of healthy specimens was probably due to the dysregulation of multiple endogenous enzymes within sera of patients with APL.

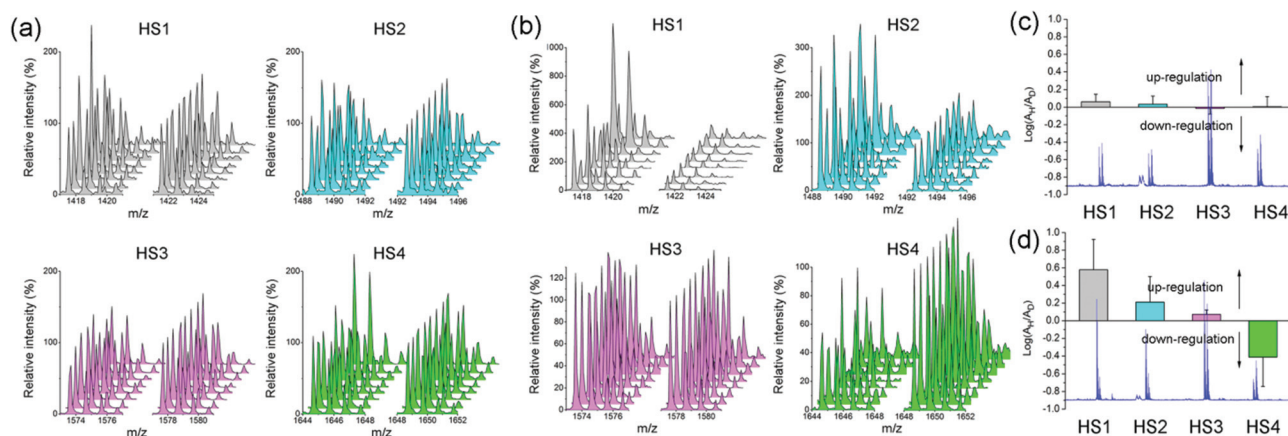


Fig. 10 Normalized MALDI-TOF MS spectra of 4 phosphopeptides enriched from the sera of (a) 8 healthy adults (light-labeled) and (b) 8 leukemia patients (light-labeled) versus the control sample (heavy-labeled). Logarithms of the isotope cluster area ratio of the 4 phosphopeptides enriched from (c) normal sera (light-labeled) to the control sera (heavy-labeled) and (d) patient sera (light-labeled) to the control sera (heavy-labeled). Embedded are representative MS spectra of (c) normal and (d) patient sera mixed with the control sera.

Conclusions

In summary, inspired by the similarity of structural units between MOAC materials (TiO_2 and Nb_2O_5) and their homogeneous 2D nanosheets (niobate and titanoniobate nanosheets), we have developed a nanocomposite of titanoniobate nanosheets embedded with Fe_3O_4 nanocrystals (Fe_3O_4 -TiNbNS) using a facile and controllable cation-exchange route, and emphasized its applicability in isolation and *in situ* isotope labeling of phosphopeptides. Through exfoliation, the 2D morphology opened up the active inner surface of the titanoniobate accessible to target molecules and outperformed conventional bulk and layered oxides in terms of phosphopeptide enrichment. Characterization showed that Fe_3O_4 nanocrystals generated *in situ* enabled the magnetic separability of the composite and played an additional role in interrupting the nanosheet restacking process so as to further expand the surface area for binding phosphopeptides. The composite nanosheet exhibited greatly improved sensitivity, selectivity and capacity in phosphopeptide enrichment, and highlighted its practicability in understanding the pathology of acute promyelocytic leukemia through relative quantification of endogenous phosphopeptides from leukemia patient sera. We envision that this magnetic 2D metal oxide nanosheet would be a powerful tool in addressing the issues that arise in biological recognition and separation.

Acknowledgements

This research was financially supported by the National Basic Research Program of China (2011CB933502), National Natural Science Foundation of China (21205060, 21335004) and the Research Fund for the Doctoral Program of Higher Education of China (20120091120029).

Notes and references

- 1 K. S. Novoselov, A. K. Geim, S. V. Morozov, D. Jiang, Y. Zhang, S. V. Dubonos, I. V. Grigorieva and A. A. Firsov, *Science*, 2004, **306**, 666–669.
- 2 X. Wang, L. J. Zhi and K. Mullen, *Nano Lett.*, 2008, **8**, 323–327.
- 3 Z. Yin, J. Zhu, Q. He, X. Cao, C. Tan, H. Chen, Q. Yan and H. Zhang, *Adv. Energy Mater.*, 2014, **4**, 1300574.
- 4 H. Wang, H. B. Feng and J. H. Li, *Small*, 2014, **10**, 2165–2181.
- 5 H. Li, J. Wu, Z. Yin and H. Zhang, *Acc. Chem. Res.*, 2014, **47**, 1067–1075.
- 6 X. Huang, Z. Zeng and H. Zhang, *Chem. Soc. Rev.*, 2013, **42**, 1934–1946.
- 7 R. Z. Ma and T. Sasaki, *Adv. Mater.*, 2010, **22**, 5082–5104.
- 8 Z. Y. Yin, H. Li, L. Jiang, Y. M. Shi, Y. H. Sun, G. Lu, Q. Zhang, X. D. Chen and H. Zhang, *ACS Nano*, 2012, **6**, 74–80.
- 9 Z. Yin, B. Chen, M. Bosman, X. Cao, J. Chen, B. Zheng and H. Zhang, *Small*, 2014, **10**, 3537–3543.
- 10 N. J. Huo, S. X. Yang, Z. M. Wei, S. S. Li, J. B. Xia and J. B. Li, *Sci. Rep.*, 2014, **4**, 5209.
- 11 Y. Zhang, B. Zheng, C. Zhu, X. Zhang, C. Tan, H. Li, B. Chen, J. Yang, J. Chen, Y. Huang, L. Wang and H. Zhang, *Adv. Mater.*, 2015, **27**, 935–939.
- 12 C. Zhu, Z. Zeng, H. Li, F. Li, C. Fan and H. Zhang, *J. Am. Chem. Soc.*, 2013, **135**, 5998–6001.
- 13 X. Peng, L. Peng, C. Wu and Y. Xie, *Chem. Soc. Rev.*, 2014, **43**, 3303–3323.
- 14 M. A. Bizeto, A. L. Shiguihara and V. R. L. Constantino, *J. Mater. Chem.*, 2009, **19**, 2512–2525.
- 15 X. G. Han, Q. Kuang, M. S. Jin, Z. X. Xie and L. S. Zheng, *J. Am. Chem. Soc.*, 2009, **131**, 3152–3153.
- 16 W. Zhou, Z. Yin, Y. Du, X. Huang, Z. Zeng, Z. Fan, H. Liu, J. Wang and H. Zhang, *Small*, 2013, **9**, 140–147.
- 17 T. Hunter, *Cell*, 2000, **100**, 113–127.
- 18 S. B. Ficarro, M. L. McClelland, P. T. Stukenberg, D. J. Burke, M. M. Ross, J. Shabanowitz, D. F. Hunt and F. M. White, *Nat. Biotechnol.*, 2002, **20**, 301–305.
- 19 S. A. Gerber, J. Rush, O. Stemman, M. W. Kirschner and S. P. Gygi, *Proc. Natl. Acad. Sci. U. S. A.*, 2003, **100**, 6940–6945.
- 20 T. S. Nuhse, A. Stensballe, O. N. Jensen and S. C. Peck, *Mol. Cell. Proteomics*, 2003, **2**, 1234–1243.
- 21 M. R. Larsen, T. E. Thingholm, O. N. Jensen, P. Roepstorff and T. J. D. Jorgensen, *Mol. Cell. Proteomics*, 2005, **4**, 873–886.
- 22 H. K. Kweon and K. Hakansson, *Anal. Chem.*, 2006, **78**, 1743–1749.
- 23 C.-T. Chen, W.-Y. Chen, P.-J. Tsai, K.-Y. Chien, J.-S. Yu and Y.-C. Chen, *J. Proteome Res.*, 2007, **6**, 316–325.
- 24 C. T. Chen and Y. C. Chen, *Anal. Chem.*, 2005, **77**, 5912–5919.
- 25 Y. Li, X. Xu, D. Qi, C. Deng, P. Yang and X. Zhang, *J. Proteome Res.*, 2008, **7**, 2526–2538.
- 26 K. Qian, J. Wan, F. Liu, H. H. Girault, B. Liu and C. Yu, *ACS Nano*, 2009, **3**, 3656–3662.
- 27 J. Wan, K. Qian, L. Qiao, Y. Wang, J. Kong, P. Yang, B. Liu and C. Yu, *Chem. – Eur. J.*, 2009, **15**, 2504–2508.
- 28 L. Hu, H. Zhou, Y. Li, S. Sun, L. Guo, M. Ye, X. Tian, J. Gu, S. Yang and H. Zou, *Anal. Chem.*, 2009, **81**, 94–104.
- 29 C. A. Nelson, J. R. Szczech, C. J. Dooley, Q. Xu, M. J. Lawrence, H. Zhu, S. Jin and Y. Ge, *Anal. Chem.*, 2010, **82**, 7193–7201.
- 30 M. Zhao, C. Deng and X. Zhang, *Chem. Commun.*, 2014, **50**, 6228–6231.
- 31 W.-F. Ma, Y. Zhang, L.-L. Li, L.-J. You, P. Zhang, Y.-T. Zhang, J.-M. Li, M. Yu, J. Guo, H.-J. Lu and C.-C. Wang, *ACS Nano*, 2012, **6**, 3179–3188.
- 32 J. H. Wu, X. S. Li, Y. Zhao, Q. A. Gao, L. Guo and Y. Q. Feng, *Chem. Commun.*, 2010, **46**, 9031–9033.
- 33 Q. Min, X. Zhang, H. Zhang, F. Zhou and J.-J. Zhu, *Chem. Commun.*, 2011, **47**, 11709–11711.
- 34 J. Lu, M. Y. Wang, Y. Li and C. H. Deng, *Nanoscale*, 2012, **4**, 1577–1580.

- 35 Y. Yan, Z. Zheng, C. Deng, Y. Li, X. Zhang and P. Yang, *Anal. Chem.*, 2013, **85**, 8483–8487.
- 36 A. Takagaki, M. Sugisawa, D. L. Lu, J. N. Kondo, M. Hara, K. Domen and S. Hayashi, *J. Am. Chem. Soc.*, 2003, **125**, 5479–5485.
- 37 A. Takagaki, C. Tagusagawa, S. Hayashi, M. Hara and K. Domen, *Energy Environ. Sci.*, 2010, **3**, 82–93.
- 38 S. J. Liang, L. R. Wen, S. Lin, J. H. Bi, P. Y. Feng, X. Z. Fu and L. Wu, *Angew. Chem., Int. Ed.*, 2014, **53**, 2951–2955.
- 39 L. Zhang, C. Hu, J. Zhang, L. Cheng, Z. Zhai, J. Chen, W. Ding and W. Hou, *Chem. Commun.*, 2013, **49**, 7507–7509.
- 40 H. N. Kim, T. W. Kim, I. Y. Kim and S.-J. Hwang, *Adv. Funct. Mater.*, 2011, **21**, 3111–3118.
- 41 V. E. Henrich and P. A. Cox, *The Surface Science of Metal Oxides*, Cambridge University Press, Cambridge, 1994.
- 42 J. C. Yu, L. Z. Zhang, Z. Zheng and J. C. Zhao, *Chem. Mater.*, 2003, **15**, 2280–2286.
- 43 H. K. Harold, *Studies in Surface Science and Catalysis*, Elsevier, Amsterdam, 1989.
- 44 Z. Sun, V. Nicolosi, D. Rickard, S. D. Bergin, D. Aherne and J. N. Coleman, *J. Phys. Chem. C*, 2008, **112**, 10692–10699.
- 45 S. Vallar, D. Houivet, J. El Fallah, D. Kervadec and J. M. Haussonne, *J. Eur. Ceram. Soc.*, 1999, **19**, 1017–1021.
- 46 N. C. Jeong, J. S. Lee, E. L. Tae, Y. J. Lee and K. B. Yoon, *Angew. Chem., Int. Ed.*, 2008, **47**, 10128–10132.
- 47 K. S. W. Sing, D. H. Everett, R. A. W. Haul, L. Moscou, R. A. Pierotti, J. Rouquerol and T. Siemieniowska, *Pure Appl. Chem.*, 1985, **57**, 603–619.
- 48 Y. Li, T. Leng, H. Lin, C. Deng, X. Xu, N. Yao, P. Yang and X. Zhang, *J. Proteome Res.*, 2007, **6**, 4498–4510.
- 49 Z. Lu, J. Duan, L. He, Y. Hu and Y. Yin, *Anal. Chem.*, 2010, **82**, 7249–7258.
- 50 L.-N. Xu, L.-P. Li, L. Jin, Y. Bai and H.-W. Liu, *Chem. Commun.*, 2014, **50**, 10963–10966.
- 51 J. L. Hsu, S. Y. Huang, N. H. Chow and S. H. Chen, *Anal. Chem.*, 2003, **75**, 6843–6852.
- 52 X. Chen, Y. Ba, L. J. Ma, X. Cai, Y. Yin, K. H. Wang, J. G. Guo, Y. J. Zhang, J. N. Chen, X. Guo, Q. B. Li, X. Y. Li, W. J. Wang, Y. Zhang, J. Wang, X. Y. Jiang, Y. Xiang, C. Xu, P. P. Zheng, J. B. Zhang, R. Q. Li, H. J. Zhang, X. B. Shang, T. Gong, G. Ning, K. Zen, J. F. Zhang and C. Y. Zhang, *Cell Res.*, 2008, **18**, 997–1006.
- 53 E. F. Petricoin, A. M. Ardekani, B. A. Hitt, P. J. Levine, V. A. Fusaro, S. M. Steinberg, G. B. Mills, C. Simone, D. A. Fishman, E. C. Kohn and L. A. Liotta, *Lancet*, 2002, **359**, 572–577.
- 54 L. M. Matrisian, G. W. Sledge Jr. and S. Mohla, *Cancer Res.*, 2003, **63**, 6105–6109.
- 55 Y. Ogata, C. J. Heppelmann, M. C. Charlesworth, B. J. Madden, M. N. Miller, K. R. Kalli, W. A. Cilby, H. R. Bergen III, D. A. Saggese and D. C. Muddiman, *J. Proteome Res.*, 2006, **5**, 3318–3325.
- 56 G. J. Zhai, X. Y. Wu, Q. Luo, K. Wu, Y. Zhao, J. A. Liu, S. X. Xiong, Y. Q. Feng, L. P. Yang and F. Y. Wang, *Talanta*, 2014, **125**, 411–417.
- 57 R. Gioia, C. Leroy, C. Drullion, V. Lagarde, G. Etienne, S. Dulucq, E. Lippert, S. Roche, F.-X. Mahon and J.-M. Pasquet, *Blood*, 2011, **118**, 2211–2221.
- 58 C. Weber, T. B. Schreiber and H. Daub, *J. Proteomics*, 2012, **75**, 1343–1356.
- 59 B. J. Druker, M. Talpaz, D. J. Resta, B. Peng, E. Buchdunger, J. M. Ford, N. B. Lydon, H. Kantarjian, R. Capdeville, S. Ohno-Jones and C. L. Sawyers, *N. Engl. J. Med.*, 2001, **344**, 1031–1037.
- 60 V. Lacronique, A. Boureux, V. DellaValle, H. Poiriel, C. T. Quang, M. Mauchauffe, C. Berthou, M. Lessard, R. Berger, J. Ghysdael and O. A. Bernard, *Science*, 1997, **278**, 1309–1312.
- 61 Q. H. Min, X. Q. Chen, X. X. Zhang and J. J. Zhu, *Lab Chip*, 2013, **13**, 3853–3861.
- 62 L. H. Hu, H. J. Zhou, Y. H. Li, S. T. Sun, L. H. Guo, M. L. Ye, X. F. Tian, J. R. Gu, S. L. Yang and H. F. Zou, *Anal. Chem.*, 2009, **81**, 94–104.
- 63 M. Levi and H. ten Cate, *N. Engl. J. Med.*, 1999, **341**, 586–592.
- 64 M. S. Tallman, P. Lefebvre, R. M. Baine, M. Shoji, I. Cohen, D. Green, H. C. Kwaan, E. Paietta and F. R. Rickles, *J. Thromb. Haemostasis.*, 2004, **2**, 1341–1350.
- 65 P. O'Mullan, D. Craft, J. Z. Yi and C. A. Gelfand, *Clin. Chem. Lab. Med.*, 2009, **47**, 685–693.